Monthly Notices
of the
ROYAL ASTRONOMICAL SOCIETY

MNRAS **480,** 2916–2928 (2018)
Advance Access publication 2018 July 25

doi:10.1093/mnras/sty1977

New Galactic Planetary nebulae selected by radio and multiwavelength characteristics

V. Fragkou,[1,2]★ Q. A. Parker,[1,2]★ I. S. Bojičić[1,2,3] and N. Aksaker[4,5]

[1]*Department of Physics, The University of Hong Kong, Hong Kong SAR, China*
[2]*Laboratory for Space Research, The University of Hong Kong, Hong Kong SAR, China*
[3]*Western Sydney University, Locked Bag 1797, Penrith South DC, NSW 1797, Australia*
[4]*Vocational School of Technical Sciences, Cukurova University, Adana 01410, Turkey*
[5]*Space Sciences and Solar Energy Research and Application center (UZAYMER), Cukurova University, Adana 01330, Turkey*

Accepted 2018 July 20. Received 2018 July 20; in original form 2018 February 19

ABSTRACT

We have used the Cornish radio catalogue combined with the use of multiwavelength data to identify 62 new Planetary Nebula (PN) candidates close to the Galactic mid-plane. Of this sample 11 have weak optical counterparts in deep narrow band Hα imaging that allows their spectroscopic follow-up. We have observed eight of these candidates spectroscopically, leading to the confirmation of seven out of eight as PNe. All but one of our sample of newly detected PNe appear to be of Type I chemistry with very large [NII]/Hα ratios. This indicates that our selection method heavily favours detection of this kind of PN. Cornish is a low-Galactic latitude survey where young objects and Type I PNe (thought to derive from higher mass progenitors) are more plentiful, but where optical extinction is large. The very high success rate in correctly identifying PNe in this zone proves the efficacy of our radio and multiple multiwavelength diagnostic tools used to successfully predict and then confirm their PN nature, at least in the cases where an optical counterpart is found and has been observed. The study reinforces the effective use of a combination of multiwavelength and optical data in the identification of new Galactic PNe and especially those of Type I chemistries whose dusty environments often prevents their easy detection in the optical regime alone.

Key words: techniques: spectroscopic – planetary nebulae: general – radio continuum: general.

1 INTRODUCTION - MULTIWAVELENGTH CHARACTERISTICS OF PLANETARY NEBULAE

Planetary Nebulae (PNe) research provides us with vital clues for understanding late stage stellar evolution of low-to-intermediate mass stars and the chemical enrichment of our Galaxy (see e.g. Frew & Parker 2010; Parker et al. 2012a). PNe are a short lived phase of late stage stellar evolution (a few tens of thousands of years) and they emit most of their energy in narrow emission lines that makes them easily detectable in narrow-band surveys and thus visible to greater distances in the Galaxy than their main-sequence counterparts. These strong emission lines also permit the determination of nebula abundances, expansion and radial velocities and, through photoionization modelling, estimations of their central star (CS) temperatures. The study of the Galactic PN population across 1–9 Gyr of stellar evolution can also trace Galactic star formation history (see Buzzoni, Arnaboldi & Corradi 2006).

The majority of PNe (more than 90 per cent; see e.g. Frew & Parker 2010) have been discovered through optical and narrow-band surveys (e.g. Drew et al. 2005; Parker et al. 2005) and reported in Parker et al. (2006), Miszalski et al. (2008) and Sabin et al. (2014). However, optical bands suffer from obscuration by interstellar dust along the line of sight, which may hide up to 90 per cent of PNe that reside on or close to the Galactic Plane and where extinction is significant (see e.g. Jacoby & Van de Steene 2004; Cohen et al. 2007a; Miszalski et al. 2008; Jacoby et al. 2010; Parker et al. 2012b). Given this and the fact that the Galactic Plane is a highly crowded area, evolved low-surface brightness PNe and distant and faint PNe are hard to detect at low-Galactic latitudes (see e.g. Sabin et al. 2010). This limitation of the optical bands can be partially solved with observations at longer wavelengths like the Infrared (IR) and at radio frequencies, which are much less affected by dust extinction (e.g. Hoare et al. 2012; Zhang, Hsia & Kwok 2012). However, spectroscopic confirmation of PN candidates uncovered at longer wavelengths is usually problematic because many lack any

★ E-mail: quentinp@hku.hk (QAP); vfrag@physics.auth.gr (VF)

obvious optical counterpart so spectroscopy at longer non-optical wavelengths would be needed.

A multiwavelength approach to PN study is also a key way to describe PN evolutionary diversity as different PN characteristics and mass components are better traced by different wavelengths (see Kwok 2010). Many past authors have used multiwavelength measurements for the identification of PNe hidden in the optical and for their discrimination from other sources that may mimic PNe, like HII regions, Supernova Remnants (SNRs), and Symbiotic Stars (e.g. Cohen & Green 2001; Cohen & Parker 2003; Cohen et al. 2007a; Corradi et al. 2008; Cohen et al. 2011; Frew & Parker 2010; Anderson et al. 2012; Parker et al. 2012b). Optical (Hα) emission traces the main PNe ionized gas component (see Kwok et al. 2008). Radio continuum emission traces the closely related free–free emission from hot ionized gas that is present in both PNe and HII regions and is usually much stronger in the second case (Anderson et al. 2012). IR emission principally maps the nebular dust component though some MIR emission is from lines such as [O IV] at 24μm (the MIR analogues of high-excitation lines in the optical such as HeII). At millimetre and sub-millimetre wavelengths emission can often be observed from molecules present in PNe (see Kwok 2000; Kwok et al. 2008) while H2 observations can also trace the molecular content in warm gas (e.g. Gledhill & Froebrich 2017). At high energies an X-ray continuum can be observed in some PNe emerging from shocked inner bubbles (e.g. Guerrero 2015).

In Section 2, we briefly describe the Cornish radio survey that serves as the base data for this paper. In Section 3, we outline our selection criteria and in Section 4, the multiwavelength diagnostic tools that have been applied to our candidates. Section 5 describes our spectroscopic observations required for the confirmation of the nature of our candidates and in Section 6, we discuss our findings. Finally, in Section 7, we summarize our results.

2 THE CORNISH RADIO SURVEY

The high-resolution, Very Large Array (VLA) Cornish radio survey (Hoare et al. 2012; Purcell et al. 2013), mapped sources emitting at 5 GHz at Galactic longitudes $l = 10^{\circ}$–65° and latitudes $\|b\| \leq 1^{\circ}$ completing the Northern coverage of the GLIMPSE survey at radio wavelengths. While 5 GHz radio observations are not sensitive to Hyper-compact H II regions (Purcell et al. 2013), the Cornish survey is ideal in detecting compact and young PNe hidden by dust in the optical bands. Hoare et al. (2012) expected to detect around 1000 PNe with some of these being new detections currently either invisible or not currently known from optical data. At frequencies equal to or more than 5 GHz it will be safe to assume that most (but not all) PNe detected at these frequencies (including from the Cornish survey) will be optically thin at this frequency. Cornish detected PNe are expected to present 5 GHz flux densities from 5 to 50 mJy for PNe of angular sizes of a few arcseconds assuming typical distances of several kpc (Hoare et al. 2012). In general, we expect these compact and likely mostly young PNe to be denser and have some optical depth.

In this work we used sources in the Cornish radio catalogue for identifying PNe candidates along the direction of the Galactic Plane that have been previously missed. Multiple multiwavelength data selection criteria to uncover PN candidates (Fig. 1a and b) were used and various discriminatory tools were applied to demonstrate the power of such multiwavelength diagnostics for uncovering new PNe by presenting confirmatory spectroscopic observations and measurements for 8 of the 11 identified PN candidates that have faint optical counterparts. Preliminary results were presented in Fragkou et al. (2017).

3 PN CANDIDATE SELECTION

For the selection of suitable PN candidates all 2637 objects from the Cornish radio catalogue (Hoare et al. 2012; Purcell et al. 2013) as obtained from the CDS VizieR service were cross-correlated with those that have IRAC counterparts (Purcell et al. (2013) quotes that 2638 sources are contained in the catalogue). No sample limits were placed on S/N (adopting the 7 sigma CORNISH catalogue limit (Purcell et al. 2013), peak flux or source angular diameter). Subsequently, the 1.4 GHz NVSS (Condon et al. 1998) and 5 GHz Cornish radio fluxes ($S_{1.4\,\mathrm{GHz}}$ and $S_{5\,\mathrm{GHz}}$) of all objects with NVSS detections available (again without imposing any S/N limits and adopting the 4 sigma NVSS catalogue limit (Condon et al. 1998) were used for calculating their spectral indices α using the relation given in Anderson et al. (2011) below:

$$\frac{S_{1.4\,\mathrm{GHz}}}{S_{5\,\mathrm{GHz}}} = \left(\frac{1.4\,\mathrm{GHz}}{5\,\mathrm{GHz}}\right)^{\alpha} \quad (1)$$

The positional uncertainty allowed in the cross-correlation of Cornish with the NVSS data was 82 arcseconds and was based on the resolution of both surveys. The NVSS resolution is ∼80 arcseconds and that of Cornish ∼1.5 arcseconds. The mean separation of matched sources between Cornish and NVSS was 10.6 arcseconds (median = 3.7 arcseconds). As stated, we expect most PNe detected in a 5 GHz survey, like Cornish, to be optically thin at that frequency with a spectral index around −0.1 expected between $S_{1.4\,\mathrm{GHz}}$ and $S_{5\,\mathrm{GHz}}$ (Hoare et al. 2012; Purcell et al. 2013). Hence, all candidates with no NVSS data or with a spectral index $\alpha < -0.5$ were excluded from our selection. This excludes non-thermal radio sources such as Supernova remnants. The flux uncertainty was not accounted for in detail in the spectral index calculation but the limit for selected sources was $\alpha < -0.5$. For optically thin sources, we expect a value around −0.1, this conservative approach takes into account the errors of the measured fluxes and the likely presence of sources that are also more optically thick. The maximum estimated error of α of all cross-correlated sources with $\alpha < -0.5$ is around 0.1 (∼20 per cent).

PNe are expected to have GLIMPSE mid-infrared [8.0 μm] - [24 μm] and [5.8 μm] - [24 μm] colour indices ranging from 3.4 to 8.7 and from 5.4 to 10.3 mag respectively (Phillips & Marquez-Lugo 2011). A cross-correlation of our candidates with the longer mid-infrared wavelength and lower resolution MIPSGAL source data at 24 μm and 70 μm Gutermuth & Heyer (2015), and again without putting any S/N limits, allowed the exclusion of objects with MIPSGAL detections whose MIR colour indices lie outside these GLIMPSE ranges. The positional uncertainty allowed in the cross-correlation of the Cornish sources with MIPSGAL sources was set to a generous 40 arcseconds, more than accounting for the resolution of both the MIPSGAL (6 arcseconds at 24 μm) and Cornish surveys. Only 16 possible matches were found within these lax allowed positional uncertainties and none when more conservative limits were imposed. As we show later, seven out of eight of the 11 candidates with optical counterparts (from all those uncovered via our original Cornish radio selection and then combined multiwavelength selection criteria) and observed spectroscopically are confirmed PN. This suggests source confusion, if present, is not significant.

Following Hoare et al. (2012), we excluded all objects with 5 GHz radio fluxes more than 110 mJy. They expected PNe at typical

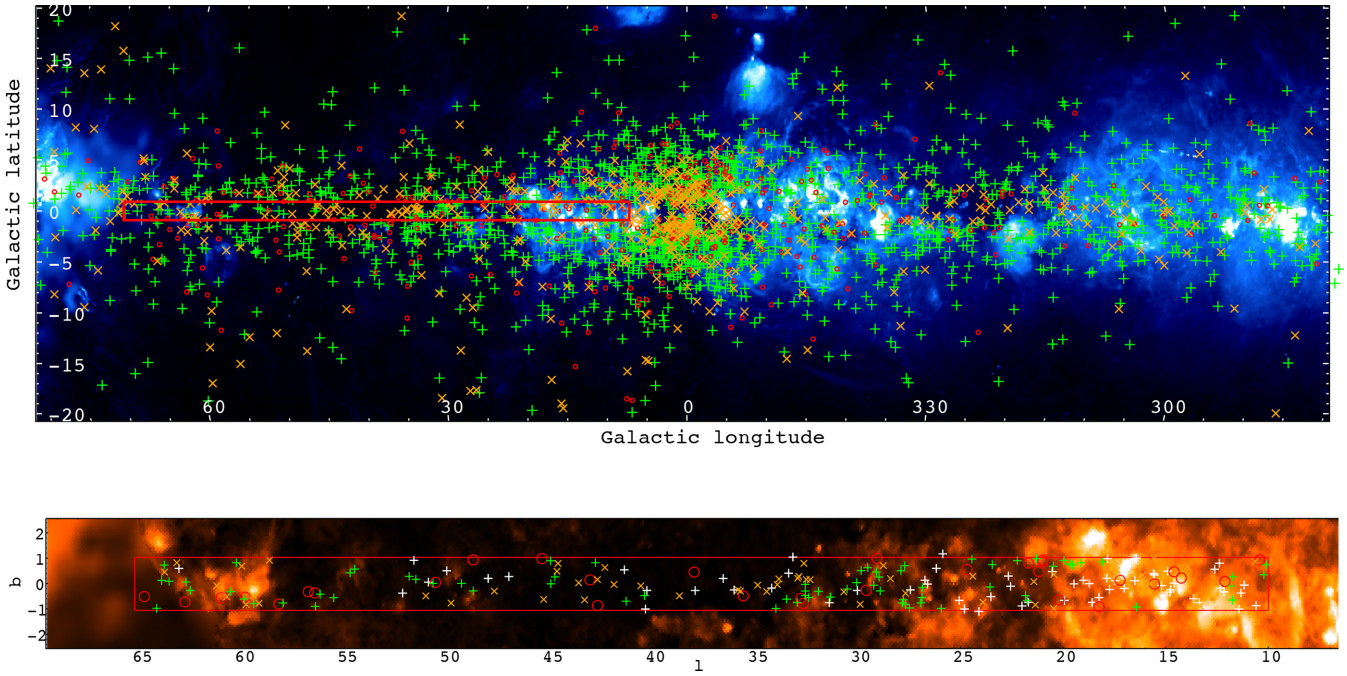

Figure 1. (a) (top): Inner Galactic Plane Hα map superimposed with all known true (green), likely (orange), and possible (red) PNe identified as such from the HASH research platform (e.g. Parker, Bojičić & Frew 2016). The inscribed small red rectangle indicates the area covered by the Cornish radio catalogue. (b) (bottom) shows an expanded plot just of the Cornish zone with the same symbols as before. In addition, the PNe candidates uncovered by this work are indicated as white "plus" signs. The data for this diagram have been provided from Finkbeiner (2003) and Parker, Frew & Bojičić (2016).

distances found via the Cornish survey to have 5 GHz radio flux densities of less than 50 mJy as much larger fluxes indicate H II regions (Filipović et al. 2009). Indeed, within our final radio selection below, only four have 5 GHz fluxes in excess of 50 mJy. It is still possible to miss a few PNe even with this conservative limit but an even larger one would add many more mainly HII regions to our sample. This would require significant amounts of additional spectroscopic follow-up with very little likely return. The very high success rate of this adopted position (the median 5 GHz radio flux of our confirmed PNe is 9.7 mJy with a maximum of 33.9 mJy while the median of the full sample of 62 objects is 16.09 mJy) indicates that an upper flux limit a bit larger than double the flux expected from Hoare et al. (2012) is a very good basis for primary selection of the best candidates.

In detail, 1463 Cornish objects are found to have NVSS counterparts and from these around 150 were excluded on the basis of their large 5 GHz fluxes (>110 mJy). A further 719 objects were excluded as a result of the imposed spectral index limit leaving 594 candidates. The cross-correlation of these remaining objects with the GLIMPSE catalogue resulted in 322 candidates. From these 11 were excluded on the basis of their [8.0 μm] - [24 μm] and [5.8 μm] - [24 μm] colour indices being clearly outside those found for known PNe. Finally, the resulting 311 radio-selected PN candidates were checked individually for extant literature data that might indicate clues as to their nature. Already identified objects (22) that most likely are not misidentifications were removed from the list (i.e. objects like H II regions and emission line stars were not removed as these could possibly be misidentifications). Of those removed 12 were known PNe, while the remaining 10 were identified as a pulsar, three masers, a galaxy, and five stars. As this is a Galactic Plane survey, stellar source confusion would always be an issue so that false stellar matches within the 5 arcsecond matching criteria are always possible though only the brighter stars in any 5 arcsecond region would have a current SIMBAD entry.

The available multiwavelength colour composite images of the remaining 289 candidates were visually examined one by one using the HASH research platform (Parker et al. 2016) where up to 40 different multiwavelength images and combinations are available from the UV to radio regimes for each source. Many are produced as "RGB" (Red, Green, Blue channel) false colour images of various optical, IR, and MIR combinations (see Parker et al. 2006 and 2017 for details). Particular attention was paid to matches with the narrow-band Hα optical data and the high-resolution UKIDSS NIR data (Lawrence et al. 2007). These RGB multiwavelength image combinations are powerful diagnostic tools in their own right as described in Parker et al. (2012b) – refer Section 4 of that paper.

Unfortunately, the majority of our PN candidates are not detected in the available optical and narrow-band images. However, based on the other non-optical, multiwavelength diagnostic indicators we have established (e.g. Frew & Parker 2010; Cohen et al. 2011 and Parker et al. 2012b) we assessed that 62 of the 289 radio selected candidates have a high chance to be PNe. This includes the example shown in Fig. 2 "FBP2", the first spectroscopically confirmed PNe from our sample listed in Table 1. We adopt the PN naming convention that has been employed by Parker et al. (2006) for the MASH PNe survey and Parker et al. (2016) for the HASH PNe surveys of the initials of the surnames of the authors and discoverers, in this case Fragkou, Bojicic and Parker. The radio data of all candidates are presented in Table 1 which includes accurate equatorial radio positions (J2000 RA/DEC), 5 GHz flux determinations with errors and the estimated radio angular diameters. All but six of these sources have angular sizes less than 3 arcseconds. From the table it is clear that a significant fraction of objects have $S_{1.4\,\mathrm{GHz}} < S_{5\,\mathrm{GHz}}$ and so seem to have some optical depth at 1.4 GHz. We find that 11 of these

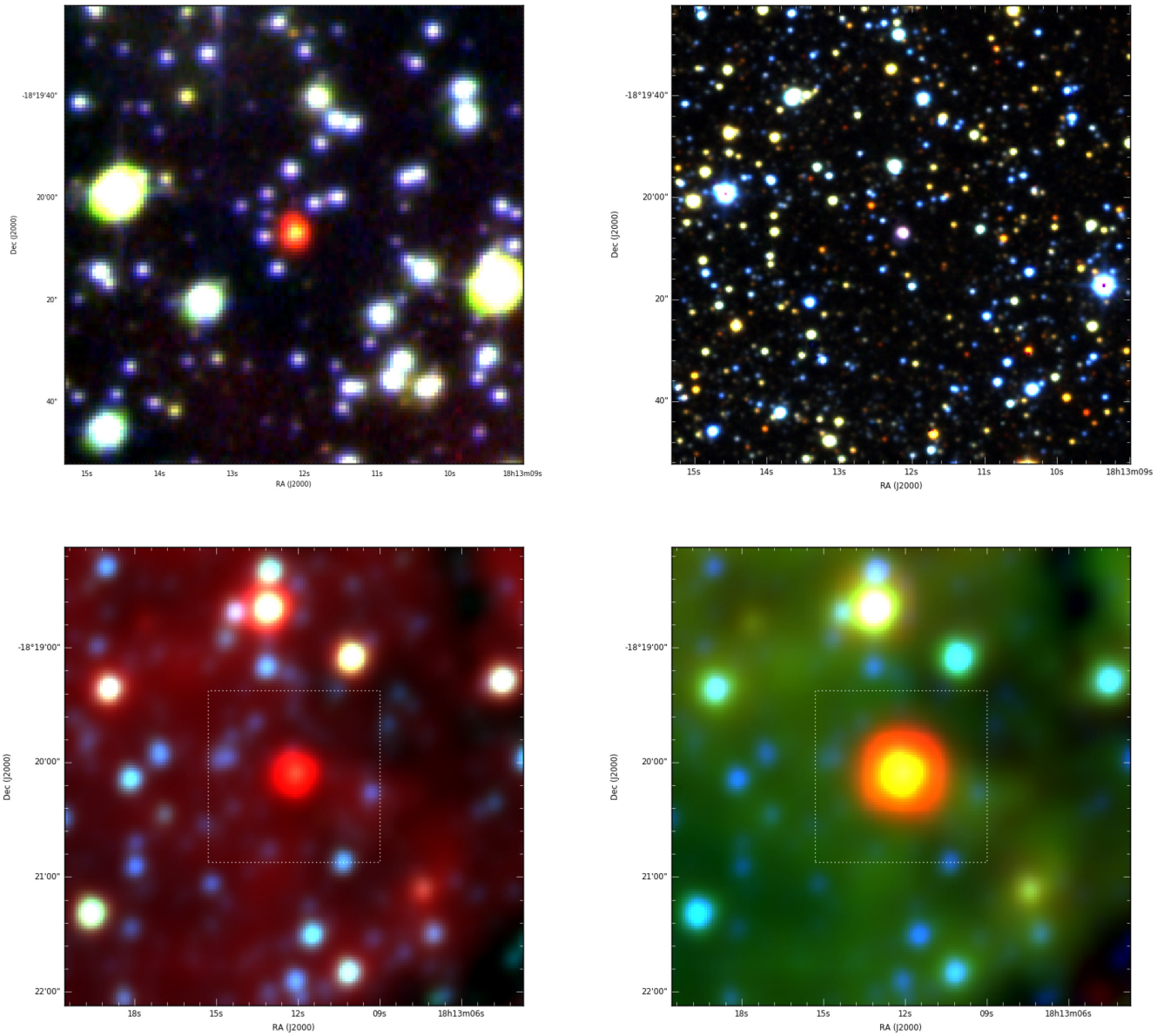

Figure 2. SHS Hα, R, and Bj band (top left), UKIDSS JHK (top right), WISE321 (bottom left), and WISE432 (bottom right) colour-composite "RGB" images of the first promising PN radio selected candidate selected in this work (designated FBP2) from the visual inspection of its multiwavelength images. It has now been confirmed spectroscopically (see Section 4) as a PN. In each combination the R, G, and B channels are assigned in the same order as listed above. It is the second object listed in Table 1. Individual survey images were provided from the HASH research platform (Parker et al. 2016).

62 tabulated colour selected candidates have weak optical counterparts with seven in the SHS (Parker et al. 2005) Southern Galactic Plane and just four solely in the IPHAS (Drew et al. 2005) Northern Galactic plane surveys. These optical detections allows their direct spectroscopic follow up. The eight sources subsequently observed spectroscopically to date are placed at the head of Table 1 and refer to, in order of increasing RA, as FBP2, FBP3, FBP4, FBP6, FBP7, FBP8, FBP9, and FBP11 and explicitly tabulated again in the spectroscopic observation log in Table 3. The remaining three sources with optical counterparts are FBP1, FBP5, and FBP10 also listed at the head of Table 1.

Apart from an initial examination of the 2MASS near-infrared (NIR) counterparts, the UKIDSS NIR survey was also examined as these newer higher resolution NIR images enabled just resolved (not stellar) sources to be identified. Our previous published work, e.g. Parker et al. (2012b), has shown that PNe tend to have distinctive combined 2MASS JHK colours and this is also true for UKIDSS which also uses the same JHK filters. Effectively every UKIDSS source had a 2MASS counterpart but not all 2MASS sources had a UKIDSS equivalent due to some gaps in coverage. Of the 289 candidates only eight UKIDSS additional sources were identified as possible PNe and they are listed separately in Table 2 along with their radio parameters. Only one candidate has a 5 GHz radio flux $>$50 mJy. None of these additional eight candidates had an optical counterpart. As these objects require further examination and more available data they have not been included in the following analysis and are not in the sample of 62 referred to throughout this paper.

We did not cross-correlate the radio selected sample with optical catalogues as we are looking for very faint emission candidates in narrow-band optical surveys and these are currently mostly

Table 1. J2000 equatorial positions (to ∼0.5 arcseconds), Cornish and NVSS radio fluxes, estimated flux errors, estimated spectral index values (with errors), and radio determined angular diameters for the 62 PN candidates revealed from this multiwavelength study. The 11 objects (including seven confirmed PNe) with optical counterparts are presented in first part of the table. Radio diameters are deconvolved FWHM values from the Cornish catalogue.

ID	RA J2000 (h:m:s)	Dec J2000 (° ′ ″)	5 GHz flux (mJy)	5 GHz flux error	1.4 GHz flux (mJy)	1.4 GHz flux error	spectral index α	α error	radio diam. (″)
FBP1	18:10:25.11	−19:18:00	102.17	12.73	25.8	1.4	1.08	0.46	10.60
FBP2	18:13:12.13	−18:20:24	33.65	3.3	–	–	–	–	1.80
FBP3	18:15:53.22	−15:45:36	8.84	1.22	–	–	–	–	1.62
FBP4	18:19:47.16	−12:57:00	15.37	1.76	2.8	0.6	1.34	1.40	1.90
FBP5	18:25:10.01	−12:18:36	6.41	1.52	–	–	–	–	2.30
FBP6	18:40:06.71	−7:42:00	9.69	1.39	–	–	–	–	1.40
FBP7	18:42:15.85	−5:00:36	5.47	0.99	–	–	–	–	1.75
FBP8	19:04:57.33	07:44:24	33.9	3.45	13.3	0.6	0.74	0.16	2.30
FBP9	19:21:27.76	15:22:48	19.51	1.85	4.3	0.5	1.19	0.64	1.75
FBP10	19:23:07.17	16:59:24	18.85	1.76	4.3	0.5	1.16	0.60	1.65
FBP11	19:48:23.27	26:49:12	5.23	1.02	–	–	–	–	1.50
FBP12	18:09:41.62	−17:49:12	19.59	1.98	3.9	0.5	1.27	0.82	1.70
FBP13	18:11:01.01	−17:44:24	17.11	1.7	19.9	5	−.12	0.02	1.57
FBP14	18:11:52.32	−19:18:36	13.82	2.41	–	–	–	–	2.30
FBP15	18:13:23.74	−18:33:36	11.97	1.42	–	–	–	–	1.10
FBP16	18:14:27.14	−19:31:12	14.58	2	7.6	0.7	0.51	0.13	1.70
FBP17	18:16:59.73	−14:10:12	16.41	2.68	7.8	0.6	0.58	0.17	2.60
FBP18	18:16:59.81	−16:15:00	4.39	1.09	–	–	–	–	1.10
FBP19	18:17:21.09	−17:23:24	19.91	3.28	–	–	–	–	3.50
FBP20	18:17:23.12	−17:42:36	9.68	1.29	4.3	1	0.64	0.30	1.70
FBP21	18:17:33.04	−15:12:00	21.91	2.13	8.5	0.7	0.74	0.19	1.66
FBP22	18:17:41.95	−15:16:12	21.92	3.22	–	–	–	–	1.40
FBP23	18:18:17.07	−16:14:24	19.77	2.57	–	–	–	–	2.50
FBP24	18:18:34.31	−15:46:12	10	1.62	–	–	–	–	1.50
FBP25	18:18:38.07	−16:15:36	18.25	2.47	–	–	–	–	1.80
FBP26	18:20:22.87	−14:31:48	15.78	2.3	–	–	–	–	3.50
FBP27	18:22:13.53	−13:41:24	9.42	1.74	–	–	–	–	2.50
FBP28	18:22:29.82	−14:13:12	13.32	2.31	–	–	–	–	1.90
FBP29	18:22:40.49	−13:16:48	23.35	2.16	–	–	–	–	1.57
FBP30	18:24:03.46	−13:36:36	59.11	5.99	43.4	1.4	0.24	0.03	4.70
FBP31	18:25:04.14	−12:37:48	107.46	10.62	–	–	–	–	1.40
FBP32	18:25:14.95	−20:11:24	34.54	3.84	–	–	–	–	1.70
FBP33	18:26:11.16	−13:18:00	8.24	0.91	–	–	–	–	1.50
FBP34	18:26:34.33	−11:58:12	18.81	1.85	–	–	–	–	1.10
FBP35	18:26:47.26	−10:48:36	15.62	1.88	10.5	0.7	0.31	0.05	1.90
FBP36	18:27:31.92	−13:05:60	7.6	1.5	9.7	2.6	−.19	0.04	2.40
FBP37	18:29:47.85	−11:51:36	14.12	1.38	–	–	–	–	1.50
FBP38	18:31:28.54	−9:00:00	14.15	1.42	3.5	0.6	1.10	0.69	1.68
FBP39	18:32:42.81	−9:16:48	32.09	3.03	–	–	–	–	1.30
FBP40	18:33:22.39	−10:20:24	36.49	6.02	–	–	–	–	4.70
FBP41	18:34:16.58	−5:45:36	31.34	4.35	22.3	0.8	0.27	0.04	2.80
FBP42	18:34:29.01	−10:07:48	14.22	1.65	11.9	2	0.14	0.03	1.40
FBP43	18:36:00.12	−8:37:12	27.22	2.69	8.8	0.7	0.89	0.27	1.70
FBP44	18:36:55.64	−5:45:00	12.38	2.18	7.1	0.6	0.44	0.12	2.60
FBP45	18:39:09.73	−8:21:36	16.4	1.55	10	0.6	0.39	0.06	1.50
FBP46	18:39:21.51	−7:19:12	30.11	2.75	5.3	0.8	1.36	1.07	1.74
FBP47	18:39:35.49	−5:28:12	13.16	1.51	–	–	–	–	1.20
FBP48	18:39:55.87	−5:39:00	69.92	7.45	70.6	2.7	−.01	–	2.20
FBP49	18:47:04.71	−2:43:48	4.54	0.94	–	–	–	–	1.62
FBP50	18:48:06.96	00:40:12	25.72	2.36	32	1.1	−.17	0.01	1.50
FBP51	18:50:45.53	00:33:36	2.62	0.65	–	–	–	–	1.50
FBP52	18:51:16.12	−1:43:48	22.66	2.29	–	–	–	–	1.60
FBP53	18:54:20.74	01:01:48	10.14	1.8	3.7	0.5	0.79	0.38	2.30
FBP54	18:57:18.51	03:18:00	13.4	2.55	13.6	0.7	−.01	–	3.20
FBP55	18:57:58.33	02:37:12	18.18	1.7	–	–	–	–	1.66
FBP56	19:01:30.32	04:18:00	32.54	2.99	–	–	–	–	1.64
FBP57	19:05:50.88	06:23:24	7.03	0.99	–	–	–	–	1.50
FBP58	19:08:36.75	06:07:12	9.12	1.48	9	0.6	0.01	–	1.90
FBP59	19:16:29.08	12:36:00	18.06	1.91	4.9	0.5	1.02	0.44	1.10
FBP60	19:18:40.35	13:27:36	6.03	0.91	5	0.5	0.15	0.03	1.65
FBP61	19:23:07.17	16:59:24	18.85	1.76	4.3	0.5	1.16	0.60	1.65
FBP62	19:28:56.07	16:51:36	22.89	2.08	36.7	1.2	−.37	0.02	1.55

Table 2. Cornish J2000 equatorial positions (the median uncertainty in RA and Dec is 0.12°), Cornish and NVSS radio fluxes and their errors, spectral index estimates and radio determined angular diameters for the eight sources of which only their UKIDSS counterpart images imply a possible PN. This includes several that appear resolved in UKIDSS (indicated with an asterisk).

ID	RA J2000 (h:m:s)	Dec J2000 (° ′ ″)	5 GHz flux (mJy)	5 GHz flux error	1.4 GHz flux (mJy)	1.4 GHz flux error	spectral index α	α error	radio diam. (″)
FBP63	18:39:09.70	−8:21:49	16.4	1.55	10.2	0.6	0.37	0.05	1.50*
FBP64	18:46:17.30	−1:40:22	49.48	4.55	5.8	0.6	1.68	1.56	2.21*
FBP65	19:02:05.60	05:40:31	62.27	6.41	11.5	0.6	1.33	0.65	1.95
FBP66	19:13:36.00	10:21:14	14.02	1.48	8.8	0.5	0.37	0.05	1.59
FBP67	19:46:10.50	26:28:01	14.27	1.36	10	0.5	0.28	0.03	1.50*
FBP68	19:47:07.60	26:28:25	5.37	0.69	4.5	0.5	0.14	0.02	1.50
FBP69	19:49:11.80	26:10:52	6.97	0.8	4.1	0.5	0.42	0.09	1.56
FBP70	19:58:38.20	27:38:24	5.57	0.66	4.8	0.6	0.12	0.02	1.50

uncatalogued. As the final candidate sample was modest in size and of small angular extent, we simply looked at the astrometric Cornish and narrow-band survey images for very close source positional co-incidences. The positional match in each case was very clear (within ∼1 arcsecond). These optical surveys have excellent astrometric integrity and positional uncertainties are typically <0.5 arcseconds (refer to the relevant publications). The SHS has 0.3 arcseconds astrometric error, (Parker et al. 2005) and IPHAS 0.5 arcseconds, (Drew et al. 2005) with 100 mas proper-motion accuracy. All selected narrow-band optical source matches are also very compact (only ∼2 arseconds across). A significant difference between the radio and optical dimensions for PNe is not expected. If these sources are mostly PNe this indicates that they are both distant and young.

Based on previous work reported in the literature by our group, e.g. see Drew et al. (2005), Cohen et al. (2007a), Cohen et al. (2011) and Parker et al. (2012b), we have found that assigning R (red), G (green), and B (blue) image channels can be very effective diagnostically in revealing promising PN candidates as shown in the following multiwavelength colour images of one of our objects FBP2 (Fig. 2). The channels are combined naturally with unit weighting and no enhancement of one channel over the other is made.

The eye (with apologies to those who are colour blind) is an excellent discriminator in this sometimes subtle process compared to solely relying on numerical photometric colour ranges. Furthermore, visual inspection can also reveal if a source is resolved (and so is a nebula and not a star) and is not a deblended element of a diffraction spike around a star (see examples in Parker et al. 2012b).

Verified PNe of moderate to low-surface brightness present as violet or pink-red colours in the NIR 2MASS and higher resolution UKIDSS J, H and Ks band images, (Skrutskie et al. 2006; Lawrence et al. 2007) due to the combinations of NIR emission lines that PNe produce at these wavelengths such as the recombination lines of Hydrogen Bracket series and He I. They present as red sources in the standard WISE321 12, 4.6, and 3.4 μm MIR band images (Wright et al. 2010); yellow in WISE432 22, 12, and 4.6 μm MIR band images (Wright et al. 2010) again to due emission lines such as [O IV] and red, orange or violet in IRAC432 8.0, 5.8, and 4.5 μm band images (see Benjamin et al. 2003; Churchwell et al. 2009). IRAC bands 3 and especially 4 sample the PAH emission, often seen in longer wavelength PNe spectra (Cohen et al. 2007a) showing an association with carbon-PNe (Cohen et al. 1989), while the IRAC 2 band is sensitive to their H2 molecular line emission (Cohen et al. 2007b). Finally, they present as red in SHS Hα, short-red and broad-band blue filter composite optical images due to the dominance of Hα that is assigned to the R channel (Parker et al. 2005; Parker et al. 2012b) and likewise for the IPHAS Hα and broad-band r' and i' (Drew et al. 2005) false-colour images.

For further clarifying the nature of our 62 candidates and their likelihood to be PNe we also employed multiwavelength photometric diagnostic tools that have been successfully used in the past for PNe identification (see e.g. Cohen et al. 2011; Parker et al. 2012b). The 8.0 μm/848 MHz fluxes of our candidates were overplotted (with big star symbols whose colours indicate their MIR/radio flux ratios) on an IRAC [5.8]-[8.0] versus [3.8]-[4.5] colour-colour plot (Fig. 3). Following Anderson et al. (2011) the MIR/radio flux ratios of our candidates were calculated after converting our Cornish 5 GHz to 848 MHz radio fluxes using the relation:

$$\frac{S_{848\mathrm{MHz}}}{S_{5\,\mathrm{GHz}}} = \left(\frac{0.848\,\mathrm{GHz}}{5\,\mathrm{GHz}}\right)^{-0.1} \quad (2)$$

for optically thin sources (see Anderson et al. 2011; Hoare et al. 2012), a condition we adopted from our selection criteria.

The MIR/radio ratio is a useful discriminator between PNe and H II regions (see Cohen & Green 2001). Our objects (indicated by red filled squares) were also plotted on 2MASS H-Ks versus J-H colour–colour plots (Fig. 4). Representatives of the most common PNe mimics (e.g. from Acker et al. 1987; Parker et al. 2006; Frew & Parker 2010), with coordinates obtained from published catalogues (Kurtz, Churchwell & Wood 1994; Giveon et al. 2005; Anderson et al. 2014; Parker et al. 2016), are also plotted on all of our colour–colour plots for illustrative purposes. We selected the same types of mimics as Cohen et al. (2011). Nine of our 62 candidates that have no measurement for all individual IRAC bands cannot be included in the corresponding IRAC colour-colour plot. Measurements of all 2MASS bands exist in published data for only 23 of our 62 candidates (refer 2MASS All-Sky Catalog of Point Sources, Cutri et al. 2003), but most of these have poor quality flags in at least one of the filters. We only include those five candidates with high quality flags in our 2MASS colour–colour plot. We note several 2MASS sources have no UKIDSS counterpart due to missing coverage.

The IRAC colour–colour plots in Fig. 3 shows our candidates generally fall in or around the black 'P' boxes, which indicate the areas centred on the median colour–colour values of confirmed PN taken from Cohen et al. (2011). The box extent is given by 3 standard errors on the mean of the colours of such confirmed PNe. Sources located in and around this box are distinctive from most other identified object types. The plot where the tightest newly confirmed PN grouping appears is Fig. 3, the IRAC [5.8]-[8.0] versus [3.8]-[4.5] colour-colour plot, but interestingly they are not inside the box. This indicates that in our flux and spectral index

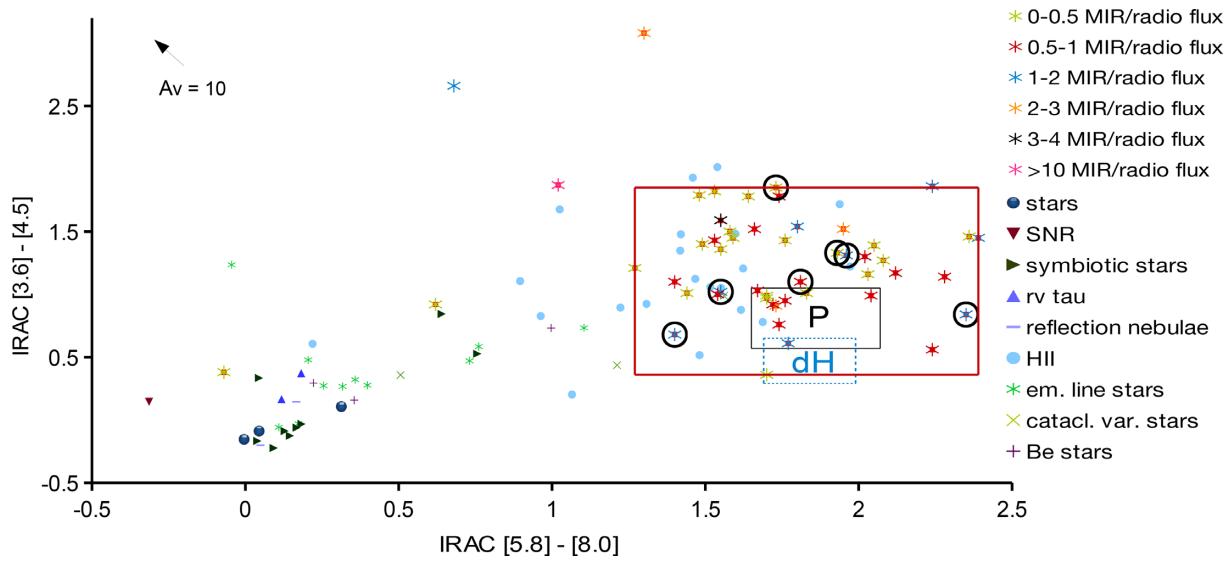

Figure 3. MIR (8.0 μm)/radio (843MHz) fluxes of our PNe candidates overplotted on an IRAC [5.8]-[8.0] versus [3.6]-[4.5] colour–colour plot. Green, red, blue, orange, black, and pink large star symbols show our PN candidates with MIR/radio flux ratios ranging from 0 to 0.5, 0.5 to 1, 1 to 2, 2 to 3, 3 to 4 and larger than 10, respectively. The black 'P' and the blue 'dH' boxes indicate the areas where most previously detected PNe and diffuse H II regions are located (see Cohen et al. 2011), while symbols for objects of different nature are indicated in the legend. A new red box indicates the suggested region in this colour-colour plane for PNe. The open black circles indicate our confirmed PNe. Coordinates of object types other than our PNe candidates are obtained from published catalogues (Kurtz et al. 1994; Giveon et al. 2005; Anderson et al. 2014; Parker et al. 2016) and cross-correlated with the GLIMPSE catalogue (Spitzer Science 2009) for finding their IRAC colours.

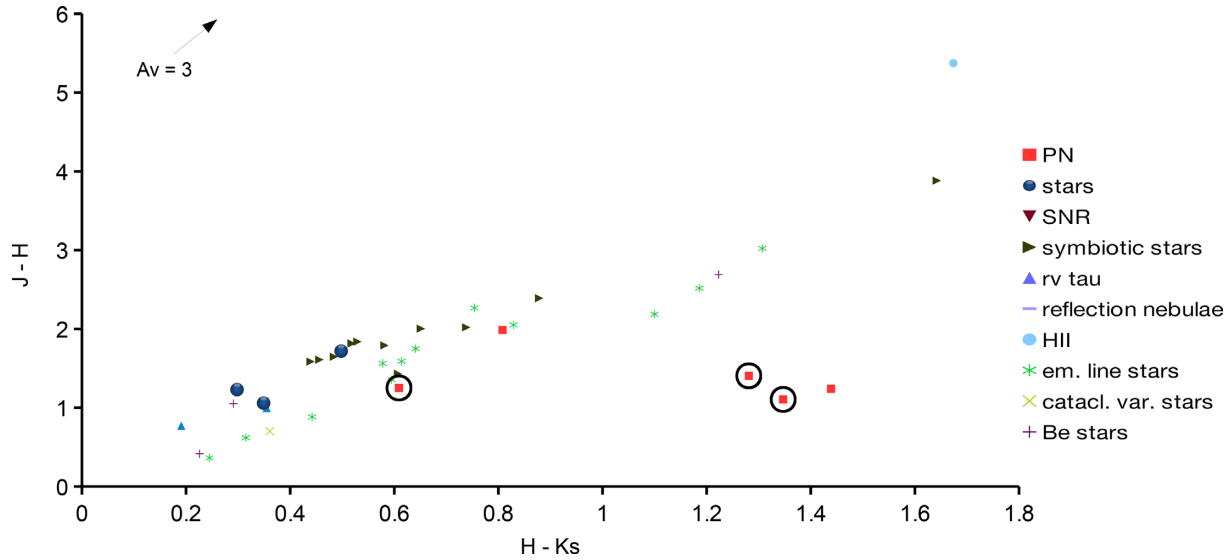

Figure 4. Our PN candidates among frequent PN mimics plotted on a 2MASS H-Ks versus J-H colour–colour plot. References and symbols are as in Fig. 3. All confirmed PNe here fall in the lower bound regions occupied by previously confirmed PNe.

limited radio samples from matched Cornish and NVSS sources the IRAC colour-colour selection should be extended in the [5.8]-[8.0] band selection from a range of approximately 1.3 to 2.4 and in the [3.8]-[4.5] band selection from 0.6 to 1.8. These new colour–colour ranges encapsulate ≈90 per cent of the radio selected sample and all of the confirmed new PNe. As we shall see below, objects in this zone may sample a different PN population type.

Based on published data (see Cohen et al. 2011) diffuse H II regions fall in the blue dH boxes (also set by the median colour value ± 3 sem). However, such diffuse H II regions are scarcely found within our radio selected samples (Kurtz et al. 1994; Giveon et al. 2005; Anderson et al. 2014), which mainly consists of compact and ultracompact H II regions that may be the most serious contaminant among our candidate objects (see Cohen et al. 2011; Anderson et al. 2012). It is also evident that more than half of our candidates have MIR/radio flux ratios between 0.5 and 10, which according to Cohen et al. (2007b, 2011), further supports their PNe nature. The 2MASS colour-colour plot in Fig. 4. shows most of our candidates with 2MASS data (only four out of 62 sources) are distributed along the horizontal (H-Ks) axis, distinguished from objects of

different nature and being in generally good agreement with the findings of Corradi et al. (2008) for 2MASS colour indices of PNe.

Determining any morphological detail for all candidates with optical counterparts is difficult as they are all compact emitters with none being more than a few arcseconds in diameter, indicating either youth and/or distance. In the Cornish images most of our candidates are very compact, while in the WISE images they mostly present a round shape as they are unresolved in these MIR surveys. Some of the UKIDSS images are resolved but their shapes are unclear beyond recognizing they are nebulae and perhaps in some case elliptical.

4 SPECTROSCOPIC CONFIRMATION OF PNE CANDIDATES

Eight of the 11 PNe candidates that have optical counterparts have now been observed spectroscopically on 1.5 to 2-m class telescopes. The three remaining are the most optically faint PNe candidates that require observations with a larger telescope. A brief log of our observations is presented in Table 3 and they are described in detail in the following subsections.

4.1 Observations

Low-dispersion, long-slit spectra were obtained for eight of our candidates. Seven were observed with the newly commissioned SpUpNIC spectrograph (see Crause et al. 2016) attached to the 1.9 m Grubb Parson telescope at South African Astronomical Observatory (SAAO) on May 24 and 27, 2017 and one with the TFOSC spectrograph on the 1.5 m Ritchey-Cretien telescope at TUBITAK National Observatory of Turkey (TUG) on July 04, 2017. For the SAAO run, the 2048 × 512 (13.5 μm pixel) E2V CCD42-10 CCD and low-dispersion grating were used covering ∼4000 to 9550Å. For the TUG run we used the 2048 × 2048 (15μm pixel side) Fairchild 447BI CCD along with a low-dispersion grism covering the wavelength region from 3230 to 9120Å. The extra coverage and system sensitivity out towards one micron with the new SpUpNIC spectrograph grating combination allows the strong far red [S III] PNe nebular lines to now be observed. The exposure times ranged from 900 to 3600 s (see Table 2) depending on the faintness of the candidates. In the case of the grism used with the TFOSC spectrograph the resolution was R=749, while for the G7 grating used with SpUpNIC spectrograph the resolution was R=700. The coordinates of the centres of the slit for each of our observations are given in Table 3. The slit width of SpUpNIC was adjusted at 2.1 arcseconds and of TFOSC at 2.4 arcseconds, while their slit lengths and orientations were 2 arcminutes East–west and 6.3 arcminutes North–South respectively. For reducing our data we adopted standard IRAF techniques. For flux calibration we observed the spectrophotometric standard stars LTT 4816, LTT 4364, and HR 8634 (Hamuy et al. 1992). For the extraction of the sky background, areas free of field stars were chosen around the centre of the slit as close as possible to the compact nebulae spectra.

4.2 Results

The long-slit spectra for eight out of our 11 PN candidates that have optical counterparts were carefully examined to confirm their nature. The spectra of seven of these displayed nebula emission lines and the absence of a continuum except for FBP6 which may have contamination from a late-type star. Relative line fluxes and absolute Hα fluxes were calculated that ranged between 1.1 and 57.5 × 10^{-15} erg cm^{-2} s^{-1} and are presented in Table 4. The calibration errors for the signal-to-noise ratio calculations are typically less than 10 per cent and are not included in Table 4. Fig. 5 illustrates the extracted 1-D spectra of all investigated objects, including identification of the key emission lines for the two spectra at the top of the combined spectral plot.

Seven out of eight of the studied objects present typical PNe emission lines in the red (and in four cases blue) region and also typical diagnostic PNe emission line ratios. In particular, the strong [NII]/Hα ratios observed for most candidates eliminate H II regions as possible contaminants while the low [S II]/Hα ratios (<0.5) eliminate Supernova remnants as contaminants. This is crucial due to the general lack of blue lines in three confirmed PNe due to extinction (FBP6, FBP7, and FBP8) preventing use in these cases of the [OIII] to H-beta ratio that is a useful PNe to H II region discriminator (see emission line ratio diagnostic plots in Frew & Parker 2010) where H II regions with [N II]/Hα>0.7 are exceedingly rare. PNe diagnostic lines include [O III] 4959, 5007Å, [N II] and Hα and the [SII] doublet 6716, 6731Å, used for determining electron densities (see e.g. Frew & Parker 2010). The [O III] blue lines are only seen in four cases and Hβ is only seen in FBP11 (the only candidate observed on the TUG 1.5 m). The observed [OIII]/Hβ line ratio is high, as expected for PNe (see Table 4), though the S/N is poor. The low-observed fluxes of the [OIII] 4959 and 5007Å lines seen in the four objects where such lines are detected are due to the strong interstellar extinction. The small departures from the canonical 2.86 [OIII] F(5007)/F(4959) expected ratio also reflects lines of poor S/N (e.g. see tab tabulated values for FBP3). Nevertheless, the observed emission lines and their ratios confirm the PN nature of the observed candidates (see e.g. Acker et al. 1989a; Frew & Parker 2010; Parker et al. 2012b). The high [N II]/Hα ratios seen in six of our confirmed PNe would be highly unusual for a random sample of PNe and also indicate that these PNe are likely of Type I chemistry (see Kingsburgh & Barlow 1994; Parker et al. 2006; Frew & Parker 2010).

The seventh object FBP11, is possibly a PNe of very high excitation with depleted [N II] and [S II] (see Parker et al. 2006; Frew & Parker 2010) despite its low S/N and low-resolution spectrum making resolving these lines difficult. The lack of HeII lines in both FBP2 and FBP3 higher S/N spectra that present He I emission imply that these two PNe are of low excitation (see Boumis et al. 2003; Zhang & Kwok 2009 though extinction could also be masking any detection; Ali et al. 2016). For three of our objects (FBP2, FBP3, FBP4) where the [S II] 6716, 6731Å doublet is present but with low-S/N ratio, a lower limit for their electron densities was estimated (see Table 4) using the STSDAS/IRAF 'temden' task (Shaw & Dufour 1995). Assuming electron temperatures $T_e = 10^4$ K (Zhang et al. 2004), the electron densities were found to be >600 cm^{-3} which is not unsurprising if they are indeed compact, young and so denser, less expanded PNe shells. No PN emission lines were found in the spectrum of FBP9. Given the presence of a continuum we consider this object's spectra is heavily contaminated by a closely adjacent star in projection. The high-resolution UKIDSS image of this source does indicate a PN-type image lurking adjacent to this star so it is also possible that the spectrograph slit missed the true source. An IFU observation should help settle the matter. These PNe candidates are not visible on the finding and guide camera and placement of the"invisible" PN candidate in the narrow slit was via relative positioning with respect to the surrounding stars.

Table 3. Log of spectroscopic Observations.

Object	Observing log				
	Slit position		Telescope	Exposure time	Date
	α (h m s)	δ (° ′ ″)		(sec)	
FBP2	18 13 12.15	− 18 20 07.31	1.9 m SAAO	900	24 May 2017
FBP3	18 15 53.20	− 15 45 53.56	1.9 m SAAO	1200	24 May 2017
FBP4	18 19 47.14	− 12 57 01.23	1.9 m SAAO	1200	24 May 2017
FBP6	18 40 06.72	− 07 41 59.80	1.9 m SAAO	1200	24 May 2017
FBP7	18 42 15.84	− 05 00 45.00	1.9 m SAAO	1200	24 May 2017
FBP8	19 04 57.40	07 44 15.18	1.9 m SAAO	1200	24 May 2017
FBP9	19 21 27.80	15 22 54.19	1.9 m SAAO	1200	24 May 2017
FBP11	19 48 23.28	26 49 26.80	1.5 m TUG	3600	04 Jul 2017

5 DISCUSSION

We found seven out of eight of our observed candidate sample to be PNe with the eighth object needing re-observation due to a closely adjacent star. Observations are still needed for the remaining three faint PN candidates in our list with optical counterparts. Our current results of PNe confirmation (possibly 100 per cent given the issues surrounding FBP9) gives confidence in our selection criteria assuming it is only extinction by intervening dust along the line of sight that prevents more optical detections. This demonstrates the power of radio and multiwavelength data in the identification of new Galactic PNe that are hidden or hard to find in the optical regime. The multiwavelength diagnostic tools applied to uncover PNe candidates and their subsequent confirmation demonstrates their excellent potential to detect new, highly obscured PNe.

Although generally PNe have [N II]/Hα line ratios <0.6 (e.g. Frew & Parker 2010), so called "Type I" PNe, first defined in Peimbert (1978) may present much stronger [N II] emission that can give [N II]/Hα ratios even larger than 6 (e.g. Kerber et al. 1998; Frew, Parker & Russeil 2006). Type I PNe are classed as having high He and N abundances (see Peimbert & Torres-Peimbert 1983) and seem to largely exhibit bipolar morphologies and high-stellar temperatures (e.g. Corradi & Schwarz 1995) and may form a distinct group originating from high-mass progenitors. The [N II]/Hα line ratios of Type I PNe from the catalogue of Maciel & Faundez-Abans (1985) range from 0.72 to 2.98 having a median value of 1.38. The [N II]/Hα line ratios for the sample were measured from the PNe line fluxes obtained from Webster (1976); Aller & Czyzak (1979); Aller, Keyes & Czyzak (1985); Peimbert & Torres-Peimbert (1987); Acker et al. (1989b); Baessgen, Diesch & Grewing (1990); Kaler et al. (1991); Kingsburgh & Barlow (1994); Perinotto et al. (1994); Kwitter & Henry (2001). The large [N II]/Hα emission line ratios (see Table 4) from our sample indicate that at least six of the seven PNe detected and confirmed in this work are likely of Type I chemistry (see e.g. Kingsburgh & Barlow 1994; Kerber et al. 1998; Frew, Parker & Russeil 2006). As all our PNe are compact the spectra are effectively integrated across the PNe so are insensitive to any positional variation in these line ratios from shocked regions. A higher resolution spectrum is needed for investigating FBP11 since the low resolution of our TUG spectrum for this object may be inadequate to resolve any [N II] emission lines if present. Our sample is highly biased in terms of selection criteria and does not reflect the chemistry of a volume limited PN sample such as that of Frew et al. (2006). However, it confirms the findings of Cohen et al. (2011) that with a low-Galactic latitude limited PN sample such as ours, where younger environments are prevalent, objects currently going through the PN phase will likely come from higher mass progenitors (Peimbert & Torres-Peimbert 1983; Karakas et al. 2009) that are also more likely to be of Type I chemistries and have bipolar morphologies. Higher resolution deep imaging of this sample would be useful to confirm this morphological assumption given the inadequacy of the current available imagery.

Our sample, though small, shows a much higher Type I PNe rate compared to normal PNe samples and furthermore these usually have bipolar morphology (Peimbert 1978; Peimbert & Torres-Peimbert 1983). It is widely known that GLIMPSE detections are biased towards PNe with high-mass progenitors (see Cohen et al. 2011) while the Cornish survey itself, from which this sample has been drawn, is at low-Galactic latitudes which sample a younger environment. Any PNe found at low-Galactic scale heights are likely to be young and so must derive from higher mass progenitors. A search of available spectra of previously identified PNe with Cornish detections using the HASH research platform, (Parker et al. 2016) reveals that from the 30 previously known PNe that are detected in Cornish, 19 (63 per cent) are of Type I chemistry. This indicates that the northern GLIMPSE region (Cornish coverage) contains more than double the high-mass progenitor PNe rate than the full GLIMPSE region (25 per cent, Cohen et al. 2011).

We expect most if not all of our detected PNe to be relatively young, as highly evolved PNe have often lost their radio emission Cohen et al. (2011). We also expect them to have more massive central stars exhibiting high-stellar temperatures as is usually the case for Type I PNe (Tylenda 1989; Cohen et al. 2007a). Their compact nature, bright IR emission and the measured relatively high electron densities of FBP2, FBP3, and FBP4 further support their early evolutionary stage (see Zhang & Kwok 1991; Miranda et al. 2010).

The absence of detectable Hβ emission line in the cases of FBP2, FBP3, FBP4, FBP6, FBP7, and FBP8 prevents us from determining the interstellar reddening from the Balmer decrement but following Ruffle et al. (2004) and using the Cornish 5 GHz radio fluxes and our measured Hα emission line fluxes, assuming an electron temperature of 10^4 K, we calculated the c(Hα) extinction of our detected PNe as:

$$c(\mathrm{H}\alpha) = log[2.85\, S_{\nu}(5\,\mathrm{GHz})/3.10 \times 10^{12} F(\mathrm{H}\alpha)] \quad (3)$$

Consequently the interstellar reddening was derived from the relation $E_{\mathrm{B-V}} \approx 1.106\mathrm{c}(\mathrm{H}\alpha)$ Pottasch (1984) and is presented in Table 4.

The compact nature of the candidates and the difficulty in determining a reliable optical angular size and Hα flux from the current

Table 4. Measured relative emission line fluxes of our seven confirmed PNe. When the Hβ line is seen as in the sole case of FBP11, the emission line ratios are calculated using the values corrected for interstellar extinction. Errors have been calculated using standard propagation.

	FBP2			FBP3			FBP4			FBP6		
Line (Å)	F[a]	I[b]	S/N[c]	F	I	S/N	F	I	S/N	F	I	S/N
[O III] 4959	8.4	–	10.7	10.1	–	1.2	9.4	–	3.7	–	–	–
[O III] 5007	26.9	–	50.2	26.7	–	5.3	45.3	–	14.7	–	–	–
[N II] 6548	48.0	–	103.5	27.1	–	16.4	12.1	–	3.6	19.7	–	5.4
Hα 6563	100	–	181.2	100	–	50.9	100	–	59.4	100	–	26.3
[N II] 6584	196.0	–	340.4	108.3	–	51.0	74.9	–	17.2	95.1	–	26.7
[S II] 6716	8.1	–	16.1	3.1	–	1.6	3.7	–	1.1	–	–	–
[S II] 6731	21.3	–	32.1	7.4	–	5.0	8.2	–	2.4	–	–	–
He I 7065	6.4	–	4.5	–	–	–	5.9	–	0.8	–	–	–
[Ar III] 7136	26.0	–	40.4	31.5	–	13.0	24.4	–	5.3	–	–	–
[O II] 7325	18.1	–	12.1	23.1	–	2.8	–	–	–	–	–	–
[Ar III] 7752	9.6	–	9.1	21.7	–	4.2	–	–	–	–	–	–
P11 8862	3.4	–	0.3	–	–	–	–	–	–	–	–	–
P10 9015	8.00	–	0.9	26.0	–	2.2	–	–	–	–	–	–
[S III] 9069	184.5	–	123.2	414.3	–	68.0	234.4	–	29.9	69.7	–	2.0
P9 9230	9.1	–	58.2	3.9	–	3.2	25.9	–	2.3	–	–	–
[S III] 9530	643.4	–	263.0	1334.2	–	136.2	575.7	–	44.1	224.7	–	12.2
5 GHz flux (mJy)		33.65 ± 3.3			8.84 ± 1.2			15.37 ± 1.8			9.69 ± 1.4	
Absolute Hα flux[d]		57.45			11.78			8.56			5.13	
F(5007)/F(4959)		3.22 ± 0.2			2.65 ± 0.9			4.80 ± 0.9			–	
F(6583)/F(6548)		4.09 ± 0.1			3.99 ± 0.3			6.18 ± 0.6			4.84 ± 1.2	
F(6716)/F(6731)		0.38 ± 0.03			0.41 ± 0.2			0.45 ± 0.3			–	
[N II]/Hα		2.44 ± 0.02			1.35 ± 0.03			0.87 ± 0.03			1.15 *pm* 0.1	
[S II]/Hα		0.29 ± 0.01			0.10 ± 0.02			0.12 ± 0.03			–	
$n_{[S\,II]}$ [e]		> 600			> 600			> 600			–	
$E_{B\text{-}V}$ (from c(Hα))		3.02 ± 0.05			3.14 ± 0.07			3.56 ± 0.06			3.58 ± 0.08	
Distance (kpc)		5.5			9.1			7.1			9.2	

	FBP7			FBP8			FBP11		
Line (Å)	F	I	S/N	F	I	S/N	F	I	S/N
Hβ 4861	–	–	–	–	–	–	2.3	35.1	2.2
[O III] 4959	–	–	–	–	–	–	3.9	51.2	3.0
[O III] 5007	–	–	–	–	–	–	11.9	141.2	8.2
[N II] 6548	90.0	–	8.9	19.1	–	5.6	–	–	–
Hα 6563	100	–	10.2	100	–	5.7	100	100	77.2
[N II] 6584	323.2	–	32.9	102.0	–	6.8	–	–	–
[S II] 6731	6.4	–	0.7	–	–	–	–	–	–
[Ar III] 7136	68.2	–	0.3	–	–	–	5.1	3.2	2.6
[S II] 9069	704.1	–	33.6	847.6	–	17.0	–	–	–
P9 9230	111.6	–	1.7	59.7	–	1.4	–	–	–
[S III] 9530	1914.8	–	92.3	3690.5	–	45.3	–	–	–
5 GHz flux (mJy)		5.47 ± 0.1			33.9 ± 3.5			5.23 ± 1.0	
Absolute Hα flux		2.32			1.07			2.50	
[O III]/Hβ		–			–			5.48 ± 1.1	
F(5007)/F(4959)		–			–			2.76 ± 0.6	
F(6583)/F(6548)		3.59 ± 0.4			5.33 ± 2.3			–	
[N II]/Hα		4.13 ± 0.3			1.21 ± 0.3			–	
[S II]/Hα		0.06 ± 0.04			–			–	
c(Hβ)[f]		–			–			3.4 ± 0.2	
$E_{B\text{-}V}$ [g]		–			–			2.62 ± 0.2	
$E_{B\text{-}V}$ (from c(Hα))		3.69 ± 0.1			4.94 ± 0.1			3.63 ± 0.1	
Distance (kpc)		10.5			5.1			11.2	

Notes: [a] Observed fluxes normalized to F(Hα)=100 and uncorrected for interstellar extinction.
[b] Observed fluxes normalized to F(Hα)=100 and corrected for interstellar extinction.
[c] Numbers represent the signal-to-noise ratio of the quoted fluxes.
[d] In units of 10^{-15} erg s^{-1} cm^{-2} arcsec^{-2}.
[e] Electron densities in units of cm^{-3}. Calculated from the F(6716)/F(6731) line ratio assuming electron temperatures of $T_e = 10^4$.
[f] Derived by c(Hβ) = 1/0.348×log((Hα/Hβ)$_{obs}$/2.85).
[g] Measured from the relation $E_{B\text{-}V} \approx 0.77$c(H$\beta$) (Osterbrock & Ferland 2006)

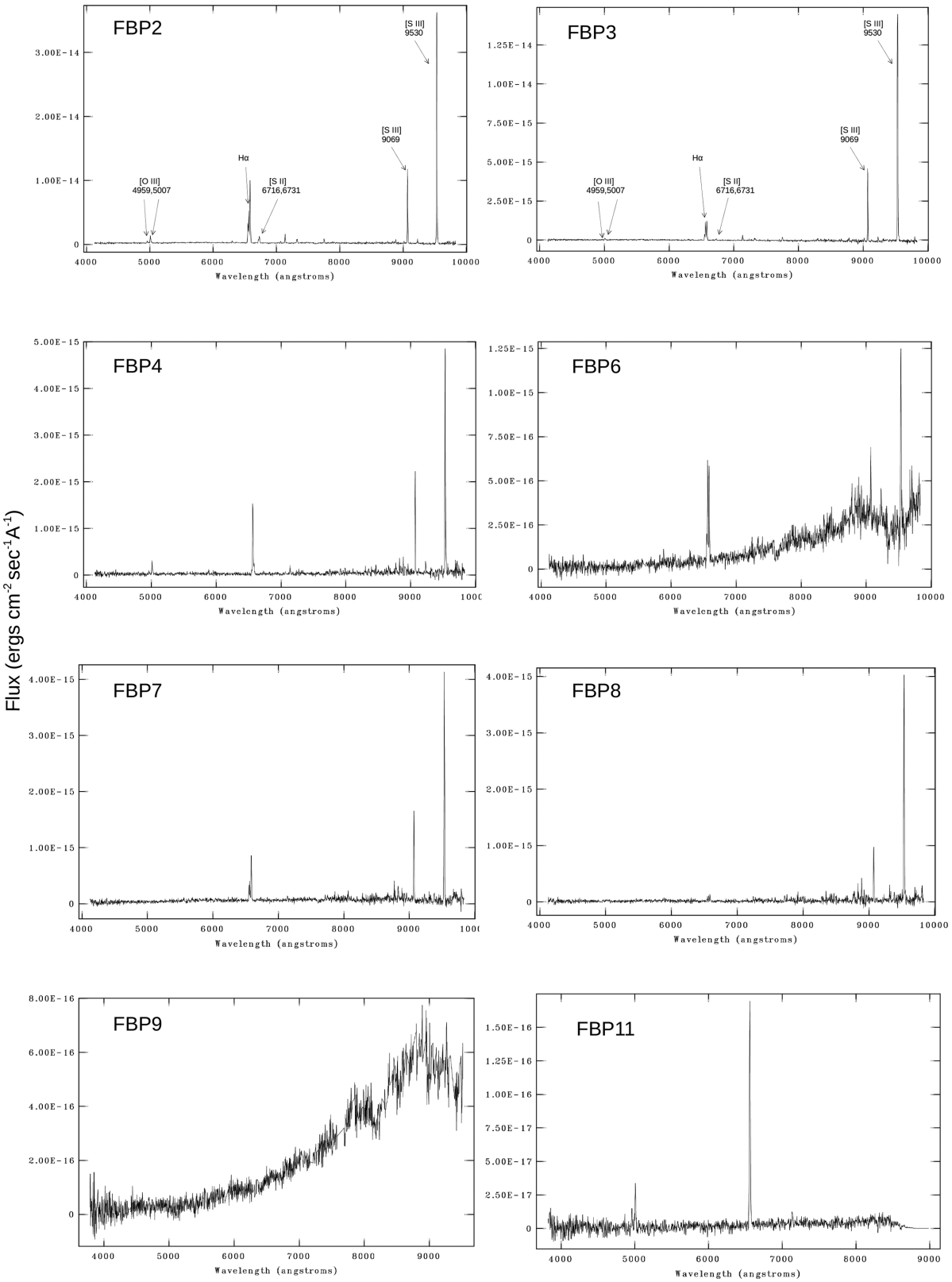

Figure 5. Long–slit low-resolution 1-D spectra of the observed objects.

data means that we cannot make any reasonable distance estimations for these PNe using the Hα surface brightness-radius (Hα-r) relation of (Frew, Parker & Bojičić 2016) or the relation by Pierce et al. (2004). However, statistical distances of our detected PNe were computed using their Cornish radio data and following van de Steene & Zijlstra (1995), and these are also presented in Table 4 but should be adopted with caution given large uncertainties in the deconvolved radio FWHM estimates.

Table 5. The measured heliocentric radial velocities of our detected PNe.

PN	Heliocentric velocity (km s^{-1})	No. fitted lines[a]
FBP2	2.4 ± 23.5	10
FBP3	− 44.9 ± 28.9	10
FBP4	60.4 ± 34.1	8
FBP6	0.0 ± 39.6	6
FBP7	53.5 ± 48.5	6
FBP8	73.6 ± 30.9	5
FBP11	− 11.6 ± 44.6	5

[a]Number of emission lines identified by the 'rvidlines' task.

Although our spectral data are of relatively low resolution, the heliocentric radial velocities of our detected PNe were measured using the NOAO/IRAF rvidlines task and are presented in Table 5. Radial velocity measurements for a radial velocity standard star (Andersen, Nordstrom & Jensen 1987) observed the same night as the first six objects (FBP2-FBP8) indicate that their accuracy is around ±25 km s^{-1}.

6 CONCLUSIONS

In this work, we have not only uncovered 62 new radio selected PNe candidates and confirmed seven as new Galactic PNe but we have also demonstrated the power of the use of multiwavelength data and diagnostics in refining their selection and detection. Most of our sample of newly detected PNe are of Type I chemistry indicating that the Cornish catalogue contains a significantly higher rate of Type I PNe than in the overall PNe population perhaps not surprising given the low-Galactic latitudes of the entire sample. Their dusty environments make the use of multiwavelength data vital for their identification.

Further investigations should reveal the nature of the three remaining Cornish multiwavelength selected PN candidates with optical detections, for which spectroscopic measurements are still missing. We confidently predict their likely PNe nature. The true status of FBP9 still needs to be confirmed though the UKIDSS data does suggest a true PN candidate is present.

ACKNOWLEDGEMENTS

This research made use of data from SuperCOSMOS Hα Survey (AAO/UKST) and the HASH research platform. We are grateful to the South African Astronomical Observatory for generous awards of telescope time for the follow-up optical spectroscopy. The first author thanks the University of Hong Kong for the provisions of a PhD scholarship. We thank the Scientific and Technological Research Council of Turkey (TUBITAK) for partial support in using the RTT 150 (Russian-Turkish 1.5-m telescope in Antalya) under project number 16BRTT150-1064.

REFERENCES

Acker A., Chopinet M., Pottasch S. R., Stenholm B., 1987, A&AS, 71, 163
Acker A., Köppen J., Samland M., Stenholm B., 1989a, The Messenger, 58, 44
Acker A., Jasniewicz G., Koeppen J., Stenholm B., 1989b, A&AS, 80, 201
Ali A., Dopita M. A., Basurah H. M., Amer M. A., Alsulami R., Alruhaili A., 2016, MNRAS, 462, 1393
Aller L. H., Czyzak S. J., 1979, Ap&SS, 62, 397
Aller L. H., Keyes C. D., Czyzak S. J., 1985, ApJ, 296, 492
Andersen J., Nordstrom B., Jensen K. S., 1987, A&AS, 68, 347
Anderson L. D., Bania T. M., Balser D. S., Rood R. T., 2011, ApJS, 194, 32
Anderson L. D., Zavagno A., Barlow M. J., García-Lario P., Noriega-Crespo A., 2012, A&A, 537, A1
Anderson L. D., Bania T. M., Balser D. S., Cunningham V., Wenger T. V., Johnstone B. M., Armentrout W. P., 2014, ApJS, 212, 1
Baessgen M., Diesch C., Grewing M., 1990, A&A, 237, 201
Benjamin R. A. et al., 2003, PASP, 115, 953
Boumis P., Paleologou E. V., Mavromatakis F., Papamastorakis J., 2003, MNRAS, 339, 735
Buzzoni A., Arnaboldi M., Corradi R. L. M., 2006, MNRAS, 368, 877
Churchwell E. et al., 2009, PASP, 121, 213
Cohen M., Green A. J., 2001, MNRAS, 325, 531
Cohen M., Parker Q. A., 2003, in Kwok S., Dopita M., Sutherland R., eds, Proc. IAU Symp. 209. Refining the UKST Hα Survey's PN Database Using MSX. Astronomical Society of the Pacific, Australia, p. 33
Cohen M., Tielens A. G. G. M., Bregman J., Witteborn F. C., Rank D. M., Allamandola L. J., Wooden D., Jourdain de Muizon M., 1989, ApJ, 341, 246
Cohen M. et al., 2007a, ApJ, 669, 343
Cohen M. et al., 2007b, MNRAS, 374, 979
Cohen M., Parker Q. A., Green A. J., Miszalski B., Frew D., Murphy T., 2011, MNRAS, 413, 514
Condon J. J., Cotton W. D., Greisen E. W., Yin Q. F., Perley R. A., Taylor G. B., Broderick J. J., 1998, AJ, 115, 1693
Corradi R. L. M., Schwarz H. E., 1995, A&A, 293, 871
Corradi R. L. M. et al., 2008, A&A, 480, 409
Crause L. et al., , 2016, in Evans C. J., Simard L., Takami H., eds, Proc. SPIE Conf. Ser. Groud-based and Airborne Instrumentation for Astronomy VI. Vol. 9908, 27
Cutri R. M. et al., 2003, VizieR On-line Data Catalog: The 2MASS All Sky Catalog of point source. 2003yCat.2246....0C
Drew J. E. et al., 2005, MNRAS, 362, 753
Filipović M. D. et al., 2009, MNRAS, 399, 769
Finkbeiner D. P., 2003, ApJS, 146, 407
Fragkou V., Bojičić I., Frew D., Parker Q., 2017, Proc. IAU Symp. 323. Planetary Nebula Candidates Uncovered with the HASH Research Platform. Kluwer, Dordrecht, p. 329
Frew D. J., Parker Q. A., 2010, PASA, 27, 129
Frew D. J., Parker Q. A., Russeil D., 2006, MNRAS, 372, 1081
Frew D. J., Parker Q. A., Bojičić I. S., 2016, MNRAS, 455, 1459
Giveon U., Becker R. H., Helfand D. J., White R. L., 2005, AJ, 130, 156
Gledhill T. M., Froebrich D., 2017, Proc. IAU Symp. 323. Planetary Nebulae in the UWISH2 Galactic Plane survey. Kluwer, Dordrecht, p. 32
Guerrero M. A., 2015, in Hamann W.-R., Sander A., Todt H. eds, Wolf-Rayer Stars: Proceedings of an International Workshop held in Potsdam, Germany, 1-5 June 2015, University of Potsdam
Gutermuth R. A., Heyer M., 2015, AJ, 149, 64
Hamuy M., Walker A. R., Suntzeff N. B., Gigoux P., Heathcote S. R., Phillips M. M., 1992, PASP, 104, 533
Hoare M. G. et al., 2012, PASP, 124, 939
Jacoby G. H., Van de Steene G., 2004, A&A, 419, 563
Jacoby G. H. et al., 2010, PASA, 27, 156
Kaler J. B., Shaw R. A., Feibelman W. A., Imhoff C. L., 1991, PASP, 103, 67
Karakas A. I., van Raai M. A., Lugaro M., Sterling N. C., Dinerstein H. L., 2009, ApJ, 690, 1130
Kerber F., Roth M., Manchado A., Groebner H., 1998, A&AS, 130, 501
Kingsburgh R. L., Barlow M. J., 1994, MNRAS, 271, 257
Kurtz S., Churchwell E., Wood D. O. S., 1994, ApJS, 91, 659
Kwitter K. B., Henry R. B. C., 2001, ApJ, 562, 804
Kwok S., 2000, The origin and evolution of Planetary Nebulae, Cambridge Univ. Press, Cambridge
Kwok S., 2010, PASA, 27, 174
Kwok S., Zhang Y., Koning N., Huang H.-H., Churchwell E., 2008, ApJS, 174, 426
Lawrence A. et al., 2007, MNRAS, 379, 1599
Maciel W. J., Faundez-Abans M., 1985, A&A, 149, 365

Miranda L. F., Vázquez R., Guerrero M. A., Pereira C. B., Iñiguez-Garín E., 2010, PASA, 27, 199
Miszalski B., Parker Q. A., Acker A., Birkby J. L., Frew D. J., Kovacevic A., 2008, MNRAS, 384, 525
Osterbrock D. E., Ferland G. J., 2006, Astrophysics of gaseous nebulae and active galactic nuclei, 2nd edn. University Science Books, Mill Valley, CA
Parker Q. A. et al., 2005, MNRAS, 362, 689
Parker Q. A. et al., 2006, MNRAS, 373, 79
Parker Q. A., Frew D. J., Acker A., Miszalski B., 2012a, Proc. IAU Symp. 283. The past, present and future of Galactic planetary nebula surveys. Kluwer, Dordrecht, p. 9
Parker Q. A. et al., 2012b, MNRAS, 427, 3016
Parker Q. A., Bojičić I. S., Frew D. J., 2016, JPhCS, 728, 032008
Peimbert M., 1978, in Terzian Y., ed., Proc. IAU Symp. 76. Chemical abundances in planetary nebulae. Kluwer, Dordrecht, p. 215
Peimbert M., Torres-Peimbert S., eds, 1983, in Proc. IAU Symp. 103. Type I planetary nebulae. Kluwer, Dordrecht, p. 233
Peimbert M., Torres-Peimbert S., 1987, RMxAA, 14, 540
Perinotto M., Purgathofer A., Pasquali A., Patriarchi P., 1994, A&AS, 107, 481
Phillips J. P., Marquez-Lugo R. A., 2011, MNRAS, 410, 2257
Pierce M. J., Frew D. J., Parker Q. A., Köppen J., 2004, PASA, 21, 334
Pottasch S. R., 1984, Astrophysics and Space Science Library. Vol. 107, Planetary nebulae - A study of late stages of stellar evolution. D. Reidel Publishing Co., Dordrecht, p. 335
Purcell C. R. et al., 2013, ApJS, 205, 1
Ruffle P. M. E., Zijlstra A. A., Walsh J. R., Gray M. D., Gesicki K., Minniti D., Comeron F., 2004, MNRAS, 353, 796
Sabin L., Zijlstra A. A., Wareing C., Corradi R. L. M., Mampaso A., Viironen K., Wright N. J., Parker Q. A., 2010, PASA, 27, 166
Sabin L. et al., 2014, MNRAS, 443, 3888
Shaw R. A., Dufour R. J., 1995, PASP, 107, 896
Skrutskie M. F. et al., 2006, AJ, 131, 1163
Spitzer Science C., 2009, VizieR Onlien Data Catalog: II/293 "GLIMPSE Source Catalog (I+II+3D)(IPAC 2008). 2293
Tylenda R., ed., 1989, Proc. IAU Symp. 131. Planetary nebulae with massive central stars. Kluwer, Dordrecht, p. 531
van de Steene G. C., Zijlstra A. A., 1995, A&A, 293, 541
Webster B. L., 1976, MNRAS, 174, 513
Wright E. L. et al., 2010, AJ, 140, 1868
Zhang C. Y., Kwok S., 1991, A&A, 250, 179
Zhang Y., Kwok S., 2009, ApJ, 706, 252
Zhang Y., Liu X.-W., Wesson R., Storey P. J., Liu Y., Danziger I. J., 2004, MNRAS, 351, 935
Zhang Y., Hsia C.-H., Kwok S., 2012, ApJ, 745, 59

This paper has been typeset from a TEX/LATEX file prepared by the author.